Supplementary Information for

Ultrasonic servoing for autonomous intraoperative robotic imaging in neurosurgery: ex-vivo experiments and medical assessment

Michael Dyck[1,2*], Arne Sachtler[2,1], Luke Dixon[3], Alexander Kirst[1], Bernhard Weber[1], Alistair Weld[4], Sophie Camp[5], Stamatia Giannarou[4,6], Alexander Dietrich[1], Julian Klodmann[1=], and Alin Albu-Schäffer[1,2=]

[*]Corresponding author. Email: michael.dyck@dlr.de

[1]German Aerospace Center (DLR), Institute of Robotics and Mechatronics, 82234 Wessling, Germany.

[2]Technical University of Munich, Department of Computer Engineering, 85748 Garching, Germany.

[3]Imperial College London, Faculty of Medicine, Division of Surgery and Cancer, and Imperial College Healthcare NHS Trust, Department of Neuroradiology, London, UK.

[4]Imperial College London, The Hamlyn Centre, London SW7 2AZ, UK.

[5]Imperial College London, Faculty of Medicine, Division of Surgery and Cancer, and Imperial College Healthcare NHS Trust, Department of Neurosurgery, London, UK.

[6]Imperial College London, Faculty of Medicine, Department of Surgery and Cancer, London SW7 2AZ, UK.

[=]These authors contributed equally.

This supplementary information shows two experimental setups in Supplementary A to additionally demonstrate the approach of this work on tissue phantoms rather than ex-vivo brain. Further, it presents in more detail the methods presented in this work in Supplementary B. This includes the ultrasonic servoing control cascade, addressing the question of how to land the ultrasound probe onto the unknown tissue, achieving perpendicular probe alignment and maintaining contact while avoiding acoustic shadowing artifacts and minimizing the interaction forces.

SUPPLEMENTARY A
PHANTOM EXPERIMENTS

Fig. S1 shows two experimental setups to additionally demonstrate the approach of this work on tissue phantoms rather than ex-vivo brain. Notation and a summary of all methods used here is explained in the main manuscript and Supplementary B. The two different ultrasound probes and tissue phantoms used in each of the experiments are presented in Figs. S1c and S1d. The UKF parameters common for all following experiments are summarized in Table S1. Initial values for the state covariance are set based on heuristically chosen values for the maximum feasible state change per Unscented Kalman Filter (UKF) iteration, that ensure smooth and slow filter convergence $\Delta \boldsymbol{p}_{max} = \begin{pmatrix} 0.001\,\mathrm{m} & 0.1\,{}^{1}\!/_{\mathrm{m}} & 0.5\,^{\circ} & 0.5\,^{\circ} \end{pmatrix}$, keeping in mind also the expected spread of the sigma points. To identify the measurement noise we performed several manual experiments, statically recording ultrasound images on different positions on the phantom, and calculating the resulting standard deviation of c and s. To be more robust against measurement noise and outliers, we specify $\sigma_{r_c}, \sigma_{r_s}$ in Table S1 conservatively, being about twice as high as the values identified manually. We set the gains for the PI controller (S37) to $k_p = 10^{-3}$ and $k_i = 10^{-5}$.

A. Linear ultrasound probe and custom-made phantom

For the first experiments, we use the lightweight, torque-controlled, seven degrees of freedom (DoF) robot arm DLR MIRO [S1] and attach a *GE 12L-RS* linear ultrasound probe via a 3D printed mechanical interface, connected to a *GE LOGIQ e* ultrasound machine. The transformation from the robot's TCP to the tip of the ultrasound probe $\boldsymbol{x}_t$ is known from CAD design. Torque sensing in all seven joints allows to directly command joint torques calculated by the impedance controller (6). For evaluation, a six DoF *ATI Mini45 Titanium* force/torque sensor between ultrasound probe and robot flange measures interaction forces during scanning. We implement the individual components of the ultrasonic servoing controller in C++, build the closed-loop system in MATLAB/Simulink and execute it on a real-time computing host. The DLR MIRO is controlled at a rate of $3\,\mathrm{kHz}$, while the ultrasound system provides data at $60\,\mathrm{Hz}$.

TABLE S1
UKF PARAMETERS, STIFFNESSES AND OTHER PARAMETERS FOR ALL EXPERIMENTS

	$\sigma_{\delta,0}$	$\sigma_{\kappa,0}$	$\sigma_{\theta,0}$	$\sigma_{\varphi,0}$	η_1	η_2	η_3
unit	m	1/m	deg	deg	-	-	-
	0.0005	0.05	0.2	0.2	1	0	3
	σ_{w_δ}	σ_{w_κ}	σ_{w_θ}	σ_{w_φ}	σ_{r_c}	σ_{r_s}	
unit	m	1/m	deg	deg	-	-	
	$\frac{\sigma_{\delta,0}}{100}$	$\frac{\sigma_{\kappa,0}}{10}$	$\frac{\sigma_{\theta,0}}{10}$	$\frac{\sigma_{\varphi,0}}{10}$	0.05	0.1	
	$\boldsymbol{k}_u$	k_d	$\boldsymbol{k}_\epsilon$	ζ	w	l	κ_p
unit	N/m	N/m	Nm/rad	-	-	m	1/m
A-A	2000	500	400	0.7	502	0.044	0
A-B	1000	500	100	0.7	800	0.032	29.4

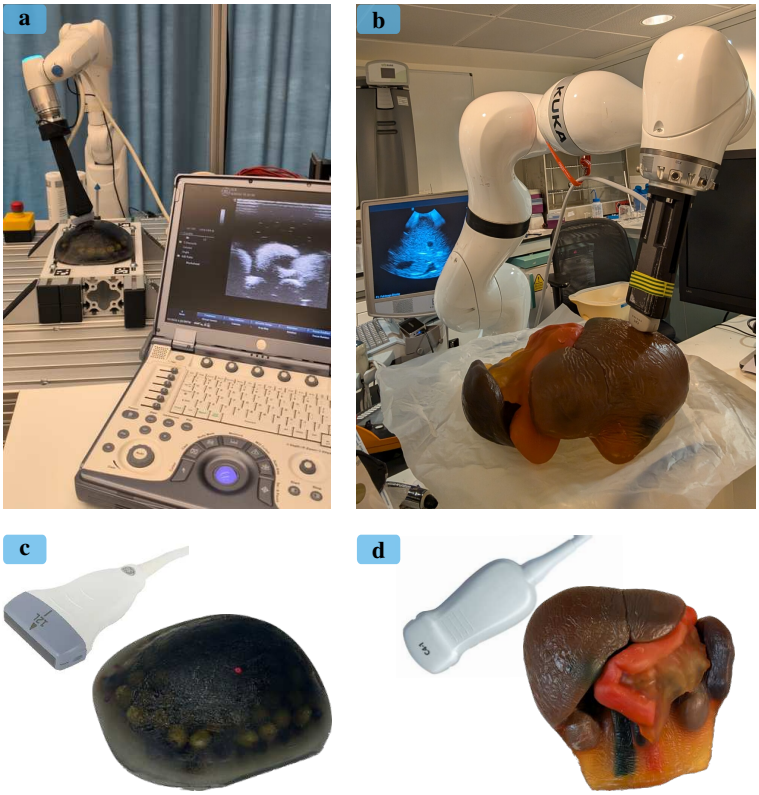


Fig. S1. **Hardware setup for phantom experiments.** The figure shows the ultrasound probe and tissue phantom used in the experiments **(a),(c)** (Supplementary A-A, DLR MIRO, linear probe, custom-made phantom), and **(b),(d)** (Supplementary A-B, KUKA LBR iiwa, convex probe, laparoscopic phantom).

Depending on the extent of visible tissue in an ultrasound image, the acoustic shadow detection algorithm, and the UKF, run at 5-10 Hz, while the PI controller (S37) runs at 100 Hz.

A custom-made phantom based on GELITA® GELATINE *Type Ballistic 3* simulates organ tissue for intraoperative ultrasound scanning. Adding glycerine increases durability of the phantom, and adjusting the water to gelatin ratio allows mimicking tissues of various stiffnesses. Inspired by [S2], different objects (olives, blueberries and flour) placed randomly into the phantom replicate the echogenic appearance and inhomogeneity of real tissue. In this experiment, we created a phantom with a water/glycerine/gelatin ratio of 19/19/2 by pouring the dissolved, preheated mixture into the negative of a custom-made convex surface of varying curvature. We use the geometry of this convex surface to evaluate the experimental performance of the ultrasonic servoing controller.

Controller stiffnesses and other parameters for this set of experiments are summarized in Table S1.

1) Acoustic coupling and interaction force: We performed two experiments, initializing the robot at the same position above an arbitrarily chosen point on the phantom and following the workflow presented in the main manuscript, Methods, section *Ultrasonic servoing control*. Results are depicted in Fig. S2, the corresponding UKF (expected) measurements are shown in Fig. S3. The two experiments differ only in the specification of $\hat{c}_{\text{des}} = 0.85$ (Figs. S2a, S3a) and $\hat{c}_{\text{des}} = 0.50$ (Figs. S2b, S3b). In Fig. S2, the first row depicts the estimated curvature $\hat{\kappa}$ alongside the rotational trajectory in β in the range of $\beta \in [-90°, 90°]$. The second row highlights the desired and actual distance $d_{u,\text{des}}, \hat{d}_u$ between ultrasound probe and estimated tissue surface, with $d_{u,\text{des}}$ calculated according to (S37) for $\hat{c}_{\text{des}} = 0.85$ and $\hat{c}_{\text{des}} = 0.5$ in left and right column, respectively. The interaction force in direction of the probe's longitudinal axis $\tilde{\boldsymbol{z}}$ measured with the dedicated force/torque sensor is visualized in the third row. Lastly, Fig. S2 shows at some exemplary points in time the ultrasound image and corresponding acoustic coupling $\boldsymbol{a}$ to illustrate the coupling performance.

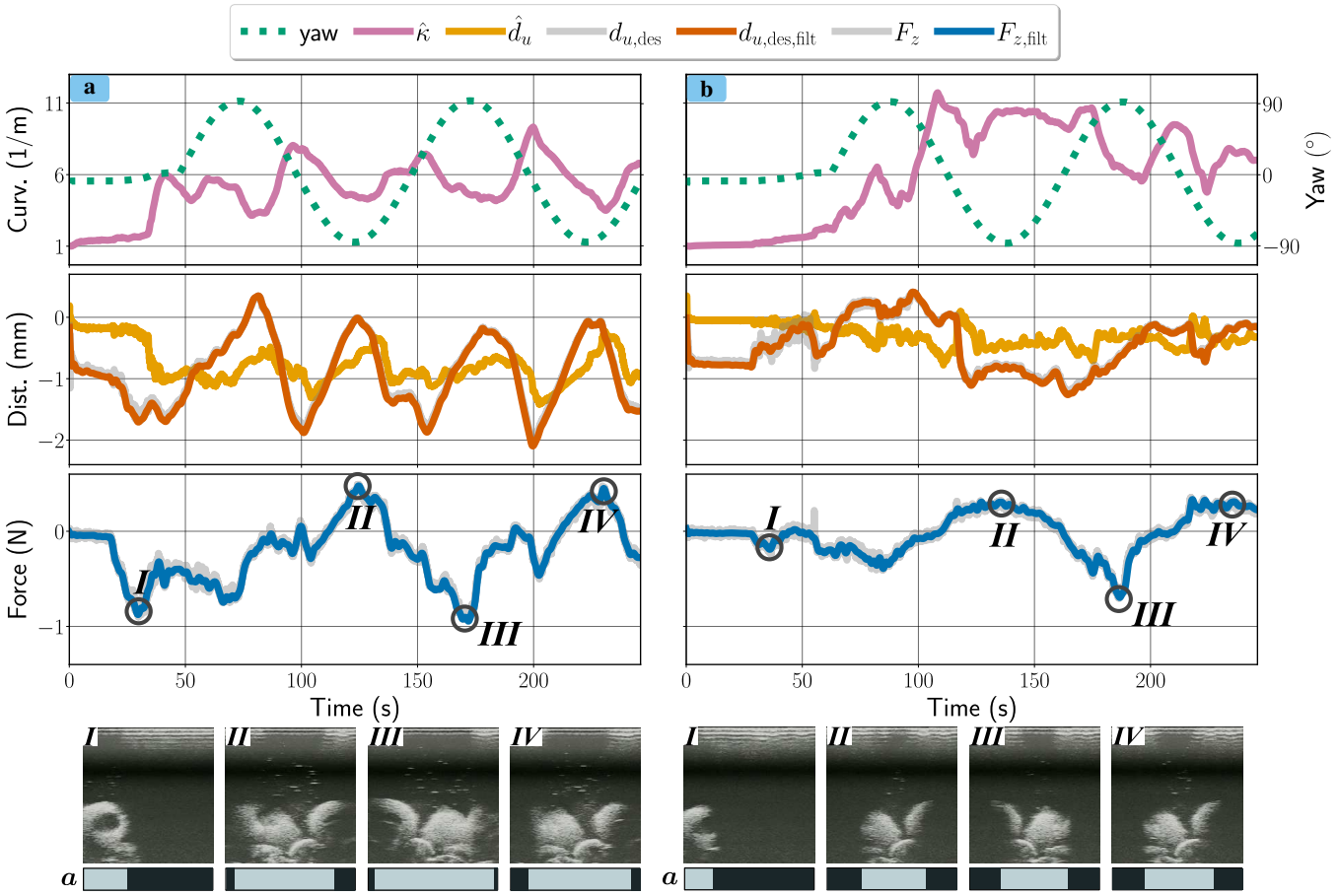


Fig. S2. **Results for the experiments Supplementary A-A1.** Plots show the probe landing on the same point on the tissue phantom surface for $\hat{c}_{\mathrm{des}} = 0.85$ (**a**) and $\hat{c}_{\mathrm{des}} = 0.50$ (**b**). Estimated curvature $\hat{\kappa}$ of and distance $\hat{d}_u$ to $\mathcal{S}_u$, desired distance $d_{u,\mathrm{des}}$ to realize a given $\hat{c}_{\mathrm{des}}$, and probe yaw rotation are mainly responsible for fluctuations in the interaction force F_z. Sample ultrasound images (***I*** - ***IV***) and the corresponding acoustic coupling $\boldsymbol{a}$ show proper coupling.

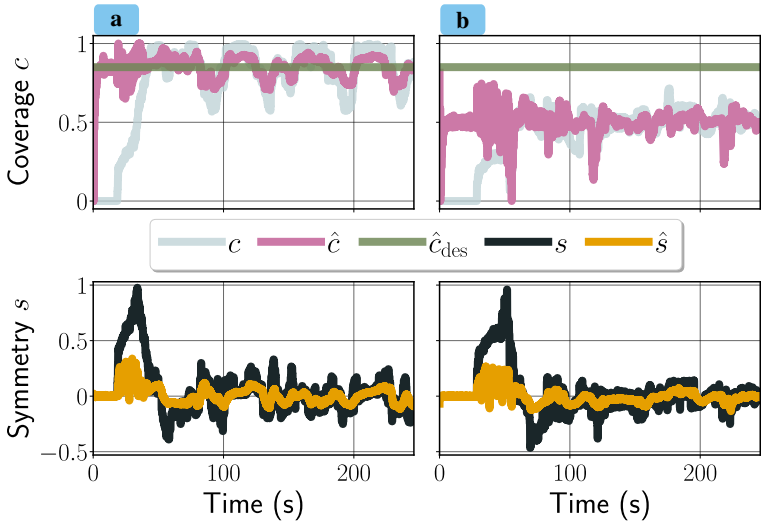


Fig. S3. **UKF measurements (c, s) and expected measurements $(\hat{c}, \hat{s})$.** Values correspond to the two experiments shown in Fig. S2 (cf. Supplementary A-A1). The two experiments differ in the value for $\hat{c}_{\mathrm{des}} = 0.85$ (**a**) and $\hat{c}_{\mathrm{des}} = 0.50$ (**b**).

The probe approaches the surface and establishes contact at around $t \approx 15\,\mathrm{s}$ and $t \approx 30\,\mathrm{s}$ for both experiments, respectively. Contact establishment is indicated by a non-zero interaction force and non-zero measurements $\boldsymbol{z}$. Right after establishing contact (cf. $\boldsymbol{I}$ in Fig. S2), the probe is oriented quickly to achieve a symmetric distribution of $\boldsymbol{a}$ across the ultrasound image, equivalent to realizing $s \approx 0$ as can be seen in the second row of Fig. S3 (remember objective $\mathrm{O}_{2.1}$). This is realized for any rotational angle β as demanded with objective $\mathrm{O}_{2.2}$, resulting in the probe aligned normal to the unknown tissue surface. Quantitatively, this is reflected in the mean value for s in both experiments (after probe alignment in the initial plane Γ, i.e., when the rotation in β starts) being $\bar{s} = 0.047$ and $\bar{s} = 0.024$, respectively.

The extent of acoustic coupling and the correlating interaction force with the tissue is dominantly influenced by the value specified for $\hat{c}_{\mathrm{des}}$. Mean interaction forces for both experiments, again taken after the initial probe alignment, as soon as the probe rotation initiates, are $\bar{F}_z = -0.197\,\mathrm{N}$ and $\bar{F}_z = -0.013\,\mathrm{N}$, respectively. Fluctuations in the measured interaction force mainly stem from changes in the estimated curvature $\hat{\kappa}$, and correspondingly changes in the distance necessary to achieve a certain c, as highlighted in the first two columns of Fig. S2. The first row in Fig. S3 confirms that, with mean values for c of $\bar{c} = 0.750 \approx \hat{c}_{\mathrm{des}} = 0.85$ and $\bar{c} = 0.420 \approx \hat{c}_{\mathrm{des}} = 0.5$. The sample ultrasound data show accurate realization of the desired coverage, where, e.g., a $\hat{c}_{\mathrm{des}} = 0.5$ results in approximately $50\ \%$ of the image showing visible tissue.

2) Local surface reconstruction: It remains to show the local surface reconstruction capabilities of the presented controller, as introduced in objective O_3. Results are shown in Fig. S4. The results in Fig. S4a come from the same experiment as was used in Fig. S2b and Fig. S3b. Fig. S4b visualizes the reconstruction performance for landing the probe on another spot on the phantom.

Both figures show the true and estimated states $\boldsymbol{p}$ and $\hat{\boldsymbol{p}}$, together with the square root of the diagonal entries of the state covariance matrix $\boldsymbol{P}_k$ as lightblue shading. The larger this lightblue area, the higher the state uncertainty at that point in time. Overall, the UKF shows good reconstruction of the local surface geometry. The second row of Fig. S4 additionally depicts the polar and azimuthal angle $\theta_{\tilde{z}}$ and $\varphi_{\tilde{z}}$ of the z-axis $\tilde{\boldsymbol{z}}$ of the ultrasound probe. With the state estimates $\hat{\theta}, \hat{\varphi}$ converging to the real solution and the ultrasound probe orientation following these estimates, i.e., $\theta_{\tilde{z}} \approx \hat{\theta}$ and $\varphi_{\tilde{z}} \approx \hat{\varphi}$, the probe is aligned normal to the tissue surface. The last row of Fig. S4 presents a zoomed in view on the trajectory of the two spherical angles of the state vector, together with the rotational trajectory around the probe's longitudinal axis. Here, the relation between β and the UKF's uncertainty on θ and φ becomes visible. Times with low

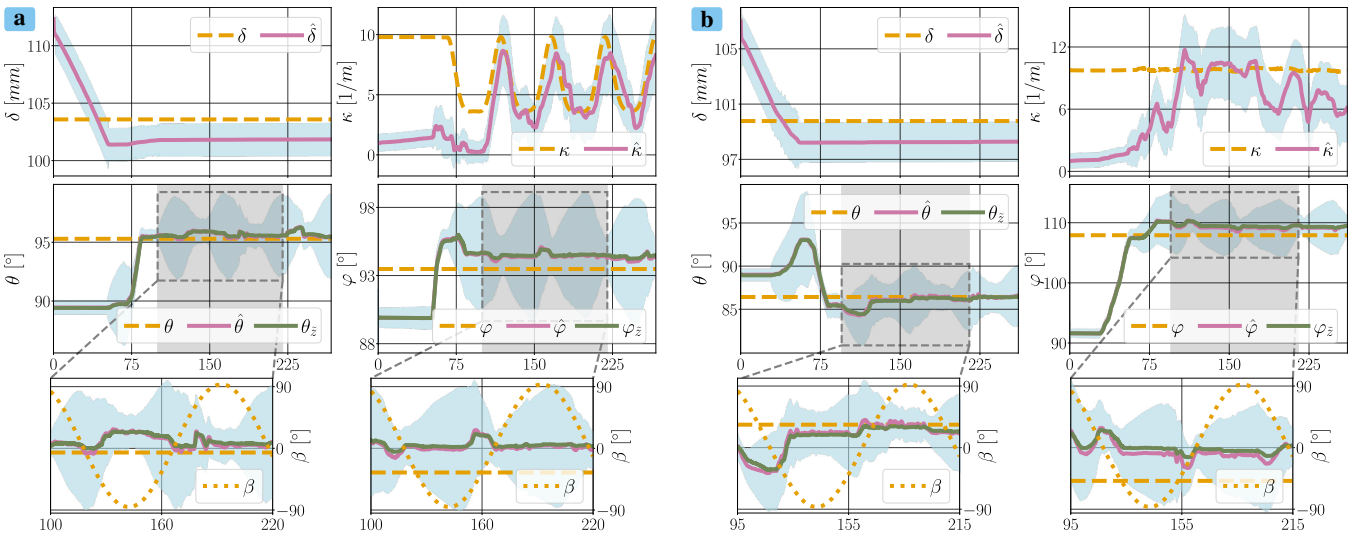


Fig. S4. **Performance evaluation of local surface reconstruction.** Plots show the convergence of the UKF estimated states $\hat{\boldsymbol{p}}$ to the true states $\boldsymbol{p}$ (cf. Supplementary A-A2) for two distinct points on the phantom (panels (**a** and **b**)). The green lines represent the polar ($\theta_{\tilde{z}}$) and azimuthal ($\varphi_{\tilde{z}}$) angle of the probe's z-axis. State uncertainty is visualized as light blue shading. The lower row shows a zoom-in view on the trajectory above, including the rotational yaw trajectory in β.

uncertainty in one of the angles correspond to high uncertainty in the other, and vice versa. This stems from the fact that the measurement $\boldsymbol{z}$ can only provide information on the probe's in-plane orientation. The uncertainty in κ does not decrease over time, as the UKF has to constantly adjust its state estimate $\hat{\kappa}$ to compensate for the probe rotation.

The remaining part is the curvature tensor according to objective $\mathrm{O}_{3.3}$. We keep track of the minimum and maximum curvature values during operation, but these will be noisy and no good estimates of the curvature tensor. Instead, we take the full history of estimated normal curvature and fit the parameters of a curvature tensor. As in (S2), let the angle α describe the orientation in the tangent plane relative to the maximum principal curvature. Neither the principal curvature directions nor their values are known, but we know it is a fixed offset β_0 from the probe's yaw orientation β. Let $\alpha = \beta - \beta_0$:

$$\kappa(\beta) = \kappa_1 \cos^2(\beta - \beta_0) + \kappa_2 \sin^2(\beta - \beta_0), \tag{S1}$$

for some unknown offset angle β_0. We formulate this as least squares problem. Take the history β_i and $\hat{\kappa}_i$ for T samples. Then,

$$L = \sum_{i=1}^{T} \left(\kappa_1 \cos^2(\beta_i - \beta_0) + \kappa_2 \sin^2(\beta_i - \beta_0) - \hat{\kappa}_i \right)^2,$$

where, $\hat{\kappa}_i$ denotes the estimated curvature at time t_i and β_i the yaw angle of the probe at the same time. We numerically solve this nonlinear least squares problem using the Trust Region Reflective algorithm [S3] and obtain $\beta_0, \kappa_1, \kappa_2 = \arg\min L(\beta_0, \kappa_1, \kappa_2)$.

Fig. S5 shows experimental results for the same experiments as before (cf. Fig. S4). The polar plots show curvature values on the radial axis over the ultrasound probe's longitudinal orientation β. The surface is curved differently at the two contact points (dashed lines in Fig. S5). We compute those curvature profiles on triangle mesh models of our surfaces using `libigl` [S4]. Solid orange lines show the history of the estimated normal curvature $\hat{\kappa}_i$ over β_i, and the blue solid line represents the curvature profile based on the fitted curvature tensor.

B. Convex ultrasound probe and laparoscopic phantom

To show the generic applicability of all components of the ultrasonic servoing controller, we perform one additional experiment using a different ultrasound machine and probe, a commercially available tissue phantom, and a different robotic manipulator. Fig. S1d shows the corresponding experimental setup. Here, we deploy the seven DoF *KUKA LBR iiwa* robot arm holding a *Zonare C4-1* convex ultrasound probe, connected to a *Zonare Z.One PRO* ultrasound machine. The commercially available *Abdominal Intraoperative & Laparoscopic Ultrasound Phantom "IOUSFAN"* by *Kyoto Kagaku Co.* serves as soft-tissue phantom. As was the case for the experiments in Supplementary A-A, the ultrasound system provides data at $60\,\mathrm{Hz}$, while the UKF operates at 5-10 Hz. The KUKA robot arm is controlled at a rate of $1\,\mathrm{kHz}$, the PI controller (S37) is again running at $100\,\mathrm{Hz}$. Table S1 lists the controller stiffnesses and remaining parameters for this experiment.

We perform one experiment equivalent to those in Supplementary A-A, landing the convex ultrasound probe onto a randomly chosen point on the liver of the IOUSFAN phantom, and initiating probe rotation after UKF convergence in the initial plane. This time, we specify $\hat{c}_{\mathrm{des}} = 0.75$. Results are depicted in Fig. S6, showing the estimated curvature, the ultrasound probe rotational trajectory, estimated and desired distance to the unknown tissue phantom surface, and true and expected measurements. Contact establishment happens at $t \approx 15\,\mathrm{s}$, probe rotation initiates shortly after. The first and second row of Fig. S6 highlight once more the strong influence of the surface's estimated normal curvature on the distance set point for the surface impedance controller. Some sample ultrasound images, now being of convex shape, taken during the experiment show good acoustic coupling. This also reflects in the mean value of $\bar{c} = 0.759 \approx \hat{c}_{\mathrm{des}}$. Furthermore, $\bar{s} = 0.073 \approx 0$ for all values of β throughout the scanning again indicates perpendicular probe alignment.

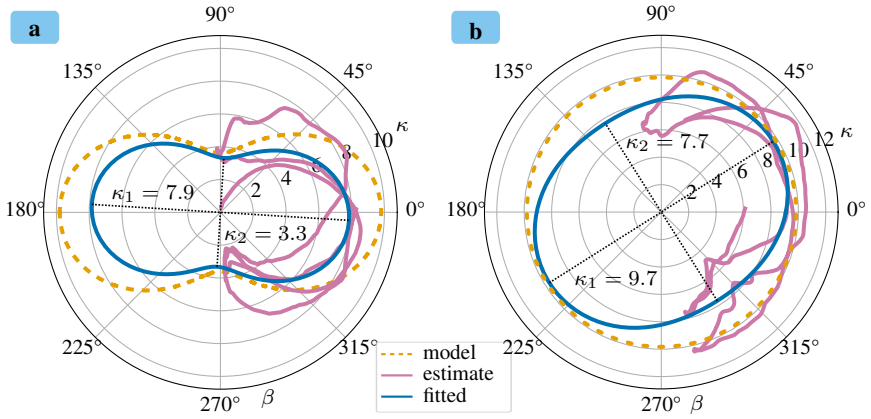


Fig. S5. **Fitted curvature tensor following** (S1)**.** The panels (**a**) and (**b**) correspond to those in Fig. S4. The polar plots show the relation of curvature κ and yaw angle β.

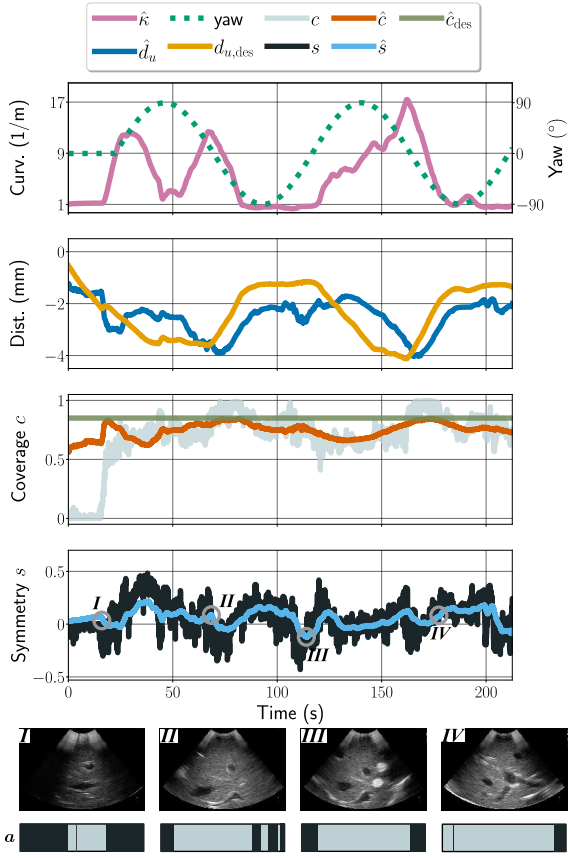


Fig. S6. **Results of the experiment Supplementary A-B.** As opposed to Supplementary A-A, convex ultrasound images are evaluated for acoustic shadow. The desired extent of contact is $\hat{c}_{\text{des}} = 0.75$.

We refrain from showing the state values in this experiment as done in Fig. S4, since no ground truth of the surface geometry of the IOUSFAN phantom was available. Still, the recorded measurements indicate convergence to the true states θ, φ. Qualitatively, also the estimated curvature $\hat{\kappa}$ depicted in Fig. S6, and correspondingly the state estimate $\hat{\delta}$, seem reasonable, as the probe was landed on the liver at a point with relatively high and low principal curvature values, respectively.

SUPPLEMENTARY B
METHODS

Going into more detail, let $\mathcal{S}_u \subset \mathbb{R}^3$ be an unknown two-dimensional surface modeling the scanned tissue, and let $\boldsymbol{\psi} \in \mathcal{S}_u$ be any desired target point of contact with the ultrasound probe. With this, we refine the high level objective O_3 of the main manuscript to be:

(O_3) Approximation of the local geometry of $\mathcal{S}_u$ around $\boldsymbol{\psi}$, i.e., identification of
- ($O_{3.1}$) the position of $\boldsymbol{\psi} \in \mathcal{S}_u \subset \mathbb{R}^3$;
- ($O_{3.2}$) the unit normal vector $\boldsymbol{n}_u(\boldsymbol{\psi})$ at $\boldsymbol{\psi}$;
- ($O_{3.3}$) the curvature tensor of $\mathcal{S}_u$ at $\boldsymbol{\psi}$.

Furthermore, given the length l of the ultrasound probe, i.e., the length of the line along which the individual transducer elements are distributed, we assume that

(A_1) the curvature of $\mathcal{S}_u$ in a circular neighborhood of radius $l/2$ around $\boldsymbol{\psi}$ is symmetric.

A. Curvature Tensor

We briefly recap the concept of (normal) curvature and the curvature tensor, needed for objective $O_{3.3}$. Consider Fig. S7a for visualizations. For a deeper introduction we recommend [S5].

Consider a point $\boldsymbol{\psi}$ on $\mathcal{S}_u$ and take an arbitrary tangent direction $\boldsymbol{X} \in \mathcal{T}_{\boldsymbol{\psi}}\mathcal{S}_u$. Intersect the surface with the plane spanned by $\boldsymbol{X}$ and the surface normal $\boldsymbol{n}(\boldsymbol{\psi})$. Locally at $\boldsymbol{\psi}$, the resulting planar curve can be described by an osculating circle, a circle of radius $r = 1/\kappa$ that best approximates the curve around $\boldsymbol{\psi}$. Here, $\kappa(\boldsymbol{X})$ is the normal curvature of $\mathcal{S}_u$ at $\boldsymbol{\psi}$ in the direction $\boldsymbol{X}$. The maximum $\kappa_1 = \max_X \kappa(\boldsymbol{X})$ and minimum $\kappa_2 = \min_X \kappa(\boldsymbol{X})$ values are called principal curvatures κ_1, κ_2 and their respective directions principal curvature directions $\boldsymbol{X}_1, \boldsymbol{X}_2$. Note that there are no unique principal curvature directions for planar (curvature-free, $\kappa_1 = \kappa_2 = 0$) or umbilical (sphere-like, $\kappa_1 = \kappa_2$) points. Principal curvature directions are always perpendicular.

Euler's Curvature Formula [S5] states that the normal curvature κ in a tangent direction $\boldsymbol{X}$ given by its angle α relative to $\boldsymbol{X}_1$ is

$$\kappa(\alpha) = \kappa_1 \cos^2(\alpha) + \kappa_2 \sin^2(\alpha). \tag{S2}$$

When varying α, the normal curvature (S2) oscillates sinusoidally between the principal curvature values κ_1 ($\alpha = 0$) and κ_2 ($\alpha = \pi/2$). We follow the sign convention of a positive curvature meaning the surface is bending away from its normal, i.e., being locally convex.

The magnitude of the normal curvature has a strong influence on how the ultrasound probe has to interact with the tissue to achieve acoustic coupling in the sense of maintaining a certain $\boldsymbol{a}^w$. As can

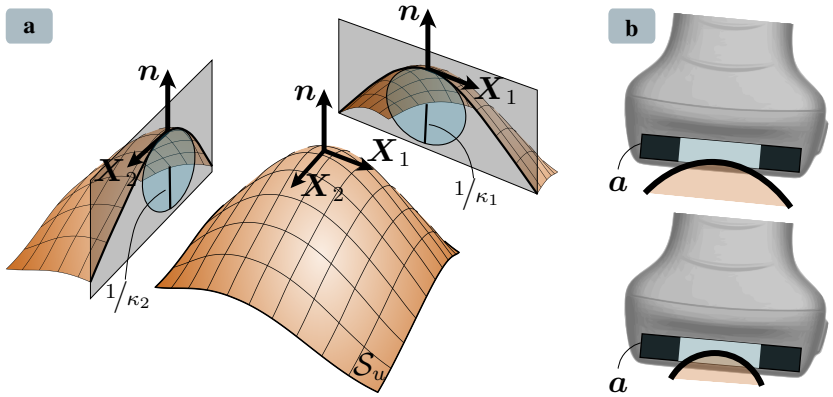


Fig. S7. **Curvature of surfaces. (a)** Principal curvature directions $\boldsymbol{X}_1, \boldsymbol{X}_2$ are those where the surface bends the most / least. The curvatures are called principal curvature values κ_1, κ_2. **(b)** The higher the normal curvature, the more the ultrasound probe needs to penetrate into the tissue to maintain the same acoustic coupling $\boldsymbol{a}$, assuming the same stiffness in all cases.

be seen in Fig. S7b, a higher normal curvature, i.e., a smaller radius for the osculating circle, requires the probe to penetrate deeper into the tissue. A higher normal curvature, i.e., a smaller radius for the osculating circle, requires the probe to penetrate deeper into the tissue.

B. Surface-centric Impedance Control

We recap details of the surface-centric impedance control [S6] that allows to control a tool relative to an arbitrary surface $\mathcal{S} \subset \mathbb{R}^3$. Let $\boldsymbol{x}_t = \begin{pmatrix} x_t & y_t & z_t \end{pmatrix}^\mathsf{T} \in \mathbb{R}^3$ be the translational component of the Cartesian forward kinematics $f_{\text{kin}} : \mathcal{Q} \to SE(3) \mid \boldsymbol{q} \mapsto \boldsymbol{x} = f_{\text{kin}}(\boldsymbol{q})$, where $\boldsymbol{q} \in \mathcal{Q}$ represent generalized configuration coordinates of the robotic manipulator. In other words, $\boldsymbol{x} \in SE(3)$ describes the pose of the ultrasound probe. The impedance controller [S6] realizes a virtual spring-damper system acting in surface-centric task coordinates (cf. Fig. S8)

$$\boldsymbol{\rho} = \begin{pmatrix} u_1(\boldsymbol{q}) \\ u_2(\boldsymbol{q}) \\ d(\boldsymbol{q}) \\ \boldsymbol{\epsilon}(\boldsymbol{q}) \end{pmatrix}, \tag{S3}$$

where u_1, u_2 are coordinates on the surface $\mathcal{S}$, d is the signed distance between the ultrasound probe and the surface, and $\boldsymbol{\epsilon}$ describes the orientational deviation from the surface normal. With the task coordinates (S3) we implement an impedance control law [S7, S8]

$$\boldsymbol{\tau} = \boldsymbol{J}_\rho^\mathsf{T}(\boldsymbol{q})[\boldsymbol{K}_\rho(\boldsymbol{\rho}_{\text{des}} - \boldsymbol{\rho}(\boldsymbol{q})) + \boldsymbol{D}_\rho(\boldsymbol{q})(\dot{\boldsymbol{\rho}}_{\text{des}} - \boldsymbol{J}_\rho(\boldsymbol{q})\dot{\boldsymbol{q}})], \tag{S4}$$

with $\boldsymbol{\tau} \in \mathbb{R}^n$ being the desired joint torques of an n-DoF, torque-controlled manipulator. $\boldsymbol{J}_\rho(\boldsymbol{q}) \in \mathbb{R}^{6\times n}$ denotes the Jacobian of $\boldsymbol{\rho}(\boldsymbol{q})$, i.e., the product $\boldsymbol{J}_\rho = \boldsymbol{J}_{\rho x}\boldsymbol{J}_x$ of the known geometrical Jacobian $\dot{\boldsymbol{x}} = \begin{bmatrix} \boldsymbol{v} & \boldsymbol{\omega} \end{bmatrix}^\mathsf{T} = \boldsymbol{J}_x(\boldsymbol{q})\dot{\boldsymbol{q}}$ and the Jacobian of $\boldsymbol{\rho}(\boldsymbol{x})$.

The surface-centric task coordinates (S3) are calculated by finding the proxy point $\boldsymbol{\chi} \in \mathcal{S}$ closest to $\boldsymbol{x}_t$. Then, $\boldsymbol{u}(\boldsymbol{\chi}) \in \mathcal{X}$ are the coordinates of this proxy point in the parameter domain $\mathcal{X} \subset \mathbb{R}^2$. $\mathcal{X}$ results from the inverse of a parametrization $\Phi : \mathcal{X} \to \mathcal{S}$. $d(\boldsymbol{q})$ represents the signed distance between ultrasound probe and proxy point. The remaining coordinates $\boldsymbol{\epsilon}(\boldsymbol{q}) \in \mathbb{R}^{3\times 1}$ are the vector part of the unit quaternion $\boldsymbol{h} = [\lambda, \boldsymbol{\epsilon}]$ describing the deviation of the ultrasound probe orientation to the normal vector

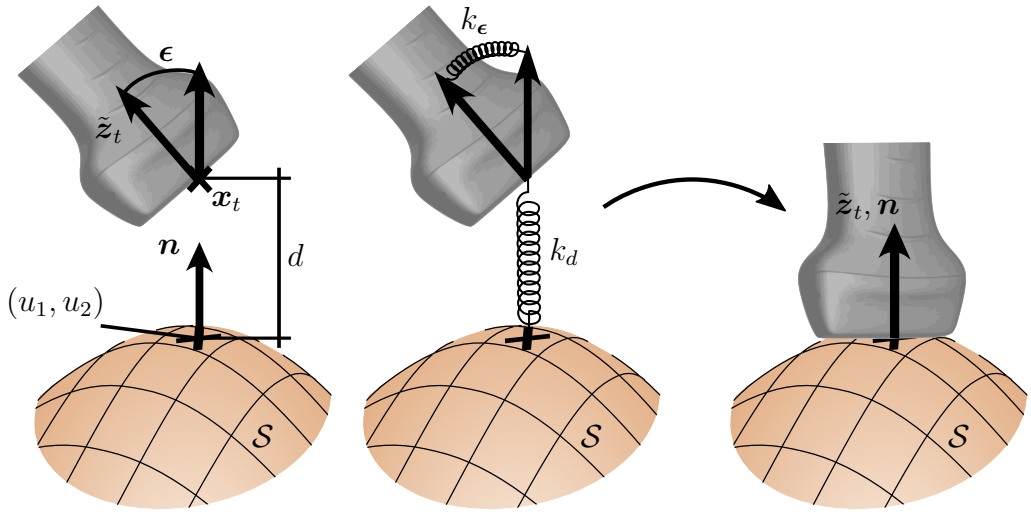


Fig. S8. **Task coordinates** (S3) **of the surface-centric impedance controller.** A virtual mass damper system pulls the ultrasound probe ($\boldsymbol{x}_t$) towards a point (u_1, u_2) on the surface $\mathcal{S}$ and aligns the probe's z-axis $\tilde{\boldsymbol{z}}_t$ with the surface normal $\boldsymbol{n}$.

$\boldsymbol{n}(\boldsymbol{\chi})$. We implement the impedance control law (S4) in these coordinates, with $\boldsymbol{K}, \boldsymbol{D}(\boldsymbol{q}) \in \mathbb{R}^{6\times6}$ being the symmetric, positive definite stiffness and damping matrices, respectively, where $\boldsymbol{K} = \operatorname{diag}\begin{pmatrix}\boldsymbol{k}_u & k_d & \boldsymbol{k}_\epsilon\end{pmatrix}$. $\boldsymbol{D}(\boldsymbol{q})$ is designed based on the damping coefficient $\zeta \in \mathbb{R}$ and double diagonalization design proposed in [S9]. The Jacobian of $\boldsymbol{\rho}(\boldsymbol{x})$ is

$$\boldsymbol{J}_{\rho x} = \frac{\partial \boldsymbol{\rho}(\boldsymbol{x})}{\partial \boldsymbol{x}} = \begin{bmatrix} \boldsymbol{J}_{uv} & \boldsymbol{0}_{2\times3} \\ \boldsymbol{J}_{dv} & \boldsymbol{0}_{1\times3} \\ \boldsymbol{J}_{\epsilon v} & \boldsymbol{J}_{\epsilon\omega} \end{bmatrix} \in \mathbb{R}^{6\times6}, \tag{S5}$$

with $\boldsymbol{v}$ and $\boldsymbol{\omega}$ denoting the translational and angular velocity vectors, respectively.

For brevity, we omit equations for the components $\boldsymbol{J}_{dv} \in \mathbb{R}^{1\times3}$ – describing the linear relation between $\boldsymbol{v}$ and velocity in the distance coordinate $\dot{d}$ – and $\boldsymbol{J}_{\epsilon\omega} \in \mathbb{R}^{3\times3}$ – representing the mapping from angular velocities $\boldsymbol{\omega}$ of the end-effector onto velocities in $\boldsymbol{\epsilon}$ (cf. [S6] for details). $\boldsymbol{J}_{uv}$ relates $\boldsymbol{v}$ to velocities in the parametrization coordinates $\boldsymbol{u}(\boldsymbol{\chi}) \in \mathcal{X}$. Calculation of this term depends upon the gradient vectors $\nabla u_1, \nabla u_2$, i.e., the directional derivatives of $\boldsymbol{u}$ for any vector tangent to the surface. Lastly, the derivation of $\boldsymbol{J}_{\epsilon v}$ requires basic concepts from differential geometry, we recommend [S5] for a visual introduction to the topic. More in-depth derivations can be found in [S6]. $\boldsymbol{J}_{\epsilon v}$ relates translational velocities $\boldsymbol{v}$ to $\dot{\boldsymbol{\epsilon}}$, stemming from the fact that any motion of the proxy point $\boldsymbol{\chi} \in \mathcal{S}$ in a tangent direction $\boldsymbol{X} \in \mathcal{T}_\chi\mathcal{S}$ changes the corresponding surface normal $\boldsymbol{n}(\boldsymbol{\chi})$ whenever the normal curvature κ_n in said direction is non-zero. The concept in differential geometry describing this relation is the *Weingarten map* [S5] $d\boldsymbol{n}(\boldsymbol{X})$. Omitting details, and using the Weingarten map and principal curvature directions $\boldsymbol{X}_1, \boldsymbol{X}_2$, we obtain

$$\boldsymbol{J}_{\epsilon v} = \boldsymbol{J}_{\epsilon\omega}[\boldsymbol{n}]_\times d\boldsymbol{n}(\boldsymbol{X}) = \boldsymbol{J}_{\epsilon\omega}[\boldsymbol{n}]_\times \boldsymbol{S}^\mathsf{T} \begin{bmatrix} \kappa_1 & 0 \\ 0 & \kappa_2 \end{bmatrix} \boldsymbol{S}, \tag{S6}$$

with $\boldsymbol{S} \in \mathbb{R}^{2\times3}$ containing $\boldsymbol{X}_1, \boldsymbol{X}_2$ as rows, and $[\boldsymbol{n}]_\times$ denoting the skew-symmetric cross product matrix of the normal vector.

Specifying $\boldsymbol{\rho}_d \in \mathbb{R}^6$ allows controlling the position of the ultrasound probe on and its distance to the surface $\mathcal{S}$, as well as the probe orientation relative to the surface normal. Perpendicular alignment of the probe is achieved by setting $\boldsymbol{\epsilon}_d = \boldsymbol{0}$. For $d_d > 0$ the robot guides the probe along the tissue without being in contact. Establishment of contact initiates at $d_d = 0$, for direct interaction with the tissue $d_d < 0$. The resulting passive contact forces depend on the value of d_d, as well as on the controller and object stiffnesses. Continuous adaption of the desired distance from, e.g., $d_d > 0 \rightarrow d_d < 0$ enables the probe to gently approach and interact with the tissue surface.

As we assume no knowledge of the pose and geometry of the unknown target surface $\mathcal{S}_u$, we define the controller surface simply to be a planar surface positioned below the object, its normal vector aligned with the z-axis of the robot's base coordinate frame, and refer to it as base surface $\mathcal{S}_b$. Think of $\mathcal{S}_b$ representing the table carrying the tissue to be scanned. Since the surface impedance control works with discretized surfaces, we represent $\mathcal{S}_b$ as a triangle mesh. We use the notation $\cdot_b, \cdot_u$ to denote quantities related to the base and target surface $\mathcal{S}_b, \mathcal{S}_u$, respectively, as visualized in Fig. S9. Now, achieving objective O_1 requires controlling the ultrasound probe to a desired distance $d_{u,\mathrm{des}}$ to $\mathcal{S}_u$ that realizes a certain desired coverage c_{des}. Similarly, perpendicular probe alignment on $\mathcal{S}_c$ (O_2) requires $\boldsymbol{\epsilon}_u = \boldsymbol{\epsilon}_{u,\mathrm{des}} = \boldsymbol{0}$. This is only possible knowing the position of $\boldsymbol{\psi} \in \mathcal{S}_u$ and the geometry of $\mathcal{S}_u$ around $\boldsymbol{\psi}$, which is precisely why we included objective O_3 in this work.

C. Local tissue surface estimation

To accomplish objective O_3 we use an observer estimating the local tissue geometry. The surface geometry observer is based on an Unscented Kalman Filter (UKF) [S10]. The UKF's current estimate is simultaneously used as the reference normal vector for the surface-centric impedance controller [S6].

As a Kalman filter, the UKF comprises a process and measurement model. We choose the UKF over the Extended Kalman Filter (EKF), as it has proven its superior performance for state estimation in nonlinear

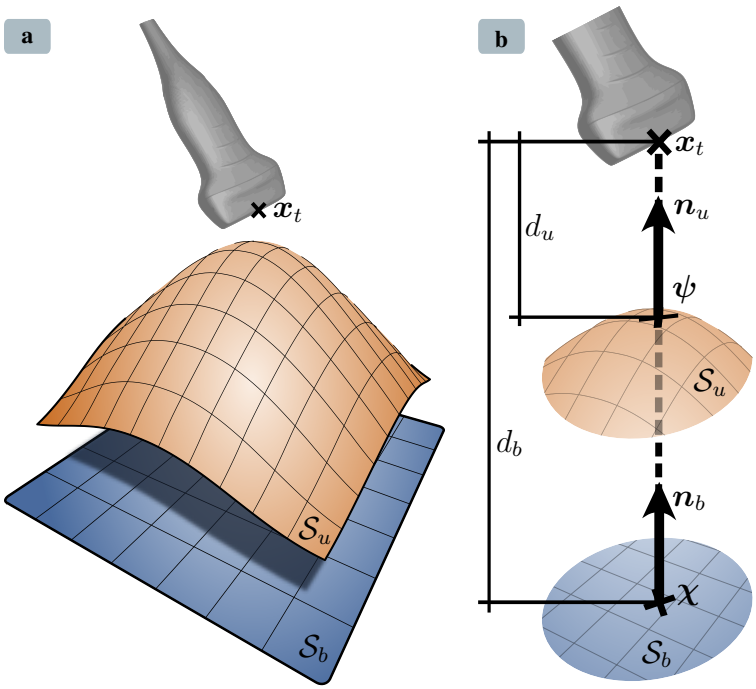


Fig. S9. **Unknown target surface and planar base surface. (a)** An ultrasound probe above the unknown target surface $\mathcal{S}_u$ and planar base surface $\mathcal{S}_b$ required for the surface impedance control. **(b)** Normal vector and distance can be defined with respect to both surfaces.

systems [S10–S12], and does not require linearization of process and measurement model, thus making it easier to implement for the given problem. We follow the notation

$$\boldsymbol{p}_k = f(\boldsymbol{p}_{k-1}, \boldsymbol{u}_{k-1}) + \boldsymbol{w}_{k-1} \tag{S7}$$

$$\boldsymbol{z}_k = h(\boldsymbol{p}_k) + \boldsymbol{v}_k. \tag{S8}$$

The process model (S7) describes how a state vector $\boldsymbol{p}_{k-1} \in \mathbb{R}^{n_p}$ at time t_{k-1} is propagated through time following a transition function f and a control input vector $\boldsymbol{u}_{k-1}$. Equation (S8) represents the measurement model, predicting the system's measurements $\boldsymbol{z}_k \in \mathbb{R}^{n_z}$ based on the estimated state $\boldsymbol{p}_k$ through the observation function h. In Kalman filtering it is assumed that, both process and measurement model, are influenced by zero-mean Gaussian noises $\boldsymbol{w}_k \sim \mathcal{N}(\boldsymbol{0}, \boldsymbol{Q}_k)$, $\boldsymbol{v}_k \sim \mathcal{N}(\boldsymbol{0}, \boldsymbol{R}_k)$ with covariances $\boldsymbol{Q}_k$, $\boldsymbol{R}_k$. Let $\boldsymbol{P}_k$ denote the current state covariance estimate. Henceforth, $\hat{\boldsymbol{p}}_k$ denotes the UKF state estimate at time t_k, as opposed to the (unknown) true state $\boldsymbol{p}_k$. We use the same notation for any quantity based on the current state estimate.

The UKF makes use of the unscented transform to approximate the distribution of a random variable propagated through a nonlinear function by again a Gaussian distribution. The posterior Gaussian is computed by generating a set of sigma points $\boldsymbol{\mathcal{P}}_i$ [S10]. Fig. S10 visualizes the idea behind the unscented transform for the example of estimating the a-priori state estimate $\hat{\boldsymbol{p}}_k^-$. In the following, we summarize the technique and UKF equations.

a) UKF equations: At each time t_k, the UKF calculates $2n_p + 1$ sigma points [S10]

$$\begin{aligned} \boldsymbol{\mathcal{P}}_{0,k-1} &= \hat{\boldsymbol{p}}_{k-1} \\ \boldsymbol{\mathcal{P}}_{i,k-1} &= \begin{cases} \hat{\boldsymbol{p}}_{k-1} + \left(\sqrt{(n_p+\lambda)\boldsymbol{P}_{k-1}}\right)_i & i = 1 \dots n_p \\ \hat{\boldsymbol{p}}_{k-1} - \left(\sqrt{(n_p+\lambda)\boldsymbol{P}_{k-1}}\right)_{i-n_p} & i = n_p+1 \dots 2n_p \end{cases} \end{aligned} \tag{S9}$$

with $\lambda = \eta_1^2(n_p + \eta_3) - n_p$ and the i-th column of the matrix square root $\left(\sqrt{\boldsymbol{P}_{k-1}}\right)_i$. Along with (S9), a

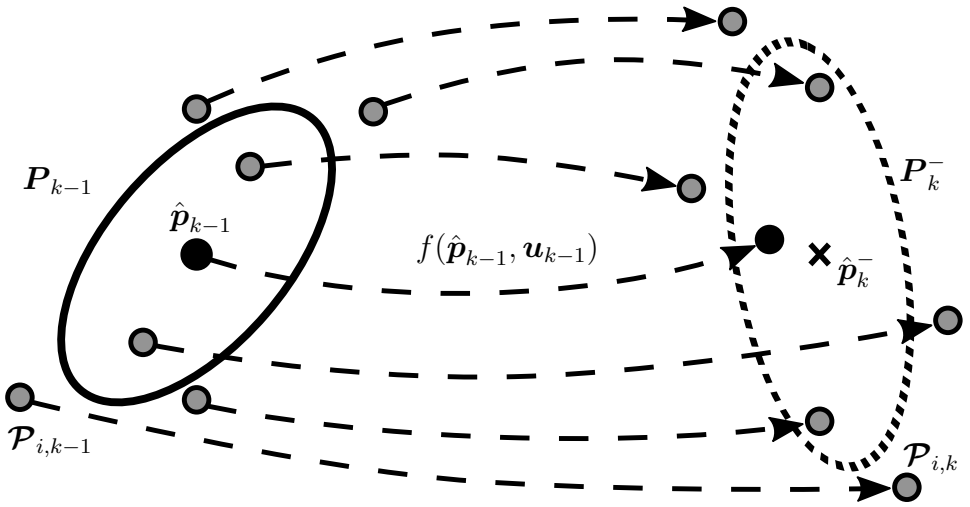


Fig. S10. **Unscented transform for the nonlinear process model** (S7)**.** The unscented transform to estimate the a-priori state estimate $\hat{\boldsymbol{p}}_k^-$ generates sigma points $\boldsymbol{\mathcal{P}}_i$, distributed around the current state estimate $\hat{\boldsymbol{p}}_{k-1}$ according to the state uncertainty $\boldsymbol{P}_{k-1}$. The process model (S7) propagates all sigma points through a transition function f using $\hat{\boldsymbol{p}}_{k-1}$ and a control input vector $\boldsymbol{u}_{k-1}$.

set of weights is calculated as

$$\begin{aligned} W_0^{(m)} &= \frac{\lambda}{n_p + \lambda}, \quad W_0^{(c)} = \frac{\lambda}{n_p + \lambda} + (1 - \eta_1^2 + \eta_2) \\ W_i^{(m)} &= W_i^{(c)} = \frac{1}{2(n_p + \lambda)}, \quad i = 1 \dots 2n_p. \end{aligned} \tag{S10}$$

Here, any prior knowledge of the distribution of $\boldsymbol{p}$ can be incorporated through the parameter η_2. With (S9),(S10), the UKF predicts a-priori estimates $\hat{\boldsymbol{p}}_k^-$ and $\boldsymbol{P}_k^-$ of the state and state covariance, respectively, by propagating each sigma point through the transition function f and calculating the resulting mean and covariance

$$\begin{aligned} \boldsymbol{\mathcal{P}}_{i,k} &= f(\boldsymbol{\mathcal{P}}_{i,k-1}, \boldsymbol{u}_{k-1}) \ \forall i \in [0, 2n_p] \\ \hat{\boldsymbol{p}}_k^- &= \sum_{i=0}^{2n_p} W_i^{(m)} \boldsymbol{\mathcal{P}}_{i,k} \\ \boldsymbol{P}_k^- &= \sum_{i=0}^{2n_p} W_i^{(c)} \left[\boldsymbol{\mathcal{P}}_{i,k} - \hat{\boldsymbol{p}}_k^-\right]\left[\boldsymbol{\mathcal{P}}_{i,k} - \hat{\boldsymbol{p}}_k^-\right]^\mathsf{T} + \boldsymbol{Q}_{k-1}. \end{aligned} \tag{S11}$$

In a second step, the UKF further propagates the sigma points $\boldsymbol{\mathcal{P}}_{i,k}$ through the observation function h to obtain an expected measurement $\hat{\boldsymbol{z}}_k$

$$\begin{aligned} \boldsymbol{\mathcal{Z}}_{i,k} &= h(\boldsymbol{\mathcal{P}}_{i,k}) \ \forall i \in [0, 2n_p] \\ \hat{\boldsymbol{y}}_k &= \boldsymbol{z}_k - \hat{\boldsymbol{z}}_k = \boldsymbol{z}_k - \sum_{i=0}^{2n_p} W_i^{(m)} \boldsymbol{\mathcal{Z}}_{i,k}. \end{aligned} \tag{S12}$$

The measurement residual $\hat{\boldsymbol{y}}_k$ describes the difference between $\hat{\boldsymbol{z}}_k$ and the actual measurement vector $\boldsymbol{z}_k$. Finally, the UKF provides a-posteriori state and covariance estimates as

$$\begin{aligned} \hat{\boldsymbol{p}}_k &= \hat{\boldsymbol{p}}_k^- + \boldsymbol{K}_k \hat{\boldsymbol{y}}_k \\ \boldsymbol{P}_k &= \boldsymbol{P}_k^- - \boldsymbol{K}_k \hat{\boldsymbol{P}}_{zz,k} \boldsymbol{K}_k^\mathsf{T}, \end{aligned} \tag{S13}$$

where the measurement residual covariance $\hat{\boldsymbol{P}}_{zz,k}$ is calculated in the same manner as is done for the a-priori state covariance in (S11). Using the estimated cross-covariance between predicted state and predicted measurement $\hat{\boldsymbol{P}}_{pz,k}$, the Kalman gain is [S10]

$$\boldsymbol{K}_k = \hat{\boldsymbol{P}}_{pz,k}\hat{\boldsymbol{P}}_{zz,k}^{-1}. \tag{S14}$$

For $\lambda = \eta_1^2(n_p+\eta_3)-n_p$, most literature suggests small positive values for η_1 (e.g., $10^{-3} \leq \eta_1 \leq 1$) and $\eta_3 = 0$ [S10, S12]. However, choosing such values leads to $\lambda < 0$ and ultimately the weights $W_i^{(m)}$ in (S10) to become negative. As a result, it is not guaranteed anymore that, even though the individual expected measurements $\boldsymbol{\mathcal{Z}}_{i,k}$ for all sigma points are constrained to the intervals $\hat{c}_{i,k} \in [0,1]$ and $\hat{s}_{i,k} \in [-1,1]$, their weighted sum (cf. (S12)) remains within these bounds. This can be ensured, however, with purely positive weights. To achieve that, we set the parameters to $\{\eta_1, \eta_2, \eta_3\} = \{1, 0, 3\}$ as suggested in [S13].

The UKF's task is to estimate the local tissue geometry around the contact point between ultrasound probe and tissue surface. As summarized in O_3 we choose to estimate the local tissue geometry up to second order, i.e., we are interested in the position of the contact point (0^{th} order), the normal vector (1^{st} order) and the curvature tensor (2^{nd} order). In the subsequent sections we specify and develop the required quantities for the UKF filter algorithm (S7), (S8): the state vector $\boldsymbol{p}$, the measurement vector $\boldsymbol{z}$, the process model f, and the measurement model h.

b) State vector: Let $\boldsymbol{\psi} \in \mathcal{S}_u$ be the point of interest where the probe at position $\boldsymbol{x}_t$ touches $\mathcal{S}_u$. Furthermore, let $\boldsymbol{\chi} \in \mathcal{S}_b$ be the corresponding proxy point on the base surface $\mathcal{S}_b$, i.e., the orthogonal projection of $\boldsymbol{x}_t$ onto $\mathcal{S}_b$. The variable $\delta \in \mathbb{R}$ in (S16) describes the signed distance of the actual tissue surface $\mathcal{S}_u$ relative to $\mathcal{S}_b$

$$\delta = \operatorname{sign}\left(\boldsymbol{n}_b(\boldsymbol{\chi}) \cdot (\boldsymbol{\psi} - \boldsymbol{\chi})\right) \|\boldsymbol{\psi} - \boldsymbol{\chi}\|_2, \tag{S15}$$

thus being the (vertical, signed) distance between the contact- $\boldsymbol{\psi}$ and proxy point $\boldsymbol{\chi}$. This is the first of the states estimating the local tissue surface $\mathcal{S}_u$ around $\boldsymbol{\psi}$ (cf. Fig. S11)

$$\boldsymbol{p} = \begin{pmatrix}\delta & \kappa & \theta & \varphi\end{pmatrix}^{\mathsf{T}} \in \mathbb{R}^4. \tag{S16}$$

The second state κ represents the normal curvature of $\mathcal{S}_u$ in the direction of the ultrasound probe scan axis. Let $\boldsymbol{\nu} \in \mathbb{R}^3$ be the unit vector representing that scan axis, i.e., the axis along which the individual sensor elements are arranged for the current β, and consider $\boldsymbol{n}_u(\boldsymbol{\psi})$ the unit normal vector at the contact point, such that $\boldsymbol{n}_u : \mathcal{S}_u \to \mathbb{S}^2$ with the unit-sphere $\mathbb{S}^2$. Then, $\Gamma = \operatorname{span}\{\boldsymbol{\nu}_{||}\,, \boldsymbol{n}_u\}$ describes the plane spanned by $\boldsymbol{\nu}_{||}$, the component of $\boldsymbol{\nu}$ tangent to $\mathcal{S}_u$ at $\boldsymbol{\psi}$, and $\boldsymbol{n}_u$. $\{\boldsymbol{\nu}_{||}, \boldsymbol{n}_u\}$ form an orthonormal basis of Γ and serve as coordinate axes of a local coordinate system $\{\mathsf{L}\}$ with origin at $\boldsymbol{\psi}$ and coordinates (γ_1, γ_2). Using the concepts introduced in Supplementary B-A, in an infinitesimal neighborhood of $\boldsymbol{\psi}$ the planar section of $\mathcal{S}_u$ obtained by intersecting the surface with the plane Γ can be described by, either the osculating circle, or a parabola satisfying (ignoring higher order terms)

$$\gamma_2 = -\frac{1}{2}\kappa\gamma_1^2, \tag{S17}$$

with the normal curvature κ of $\mathcal{S}_u$ in the direction of $\boldsymbol{\nu}$. Lastly, θ and φ are the spherical coordinates (cf. Fig. 7E), more precisely the polar and azimuthal angle, of $\boldsymbol{n}_u(\boldsymbol{\psi})$. To avoid the pole singularity at $\boldsymbol{n}_u = \begin{pmatrix}0 & 0 & 1\end{pmatrix}^{\mathsf{T}}$ (arbitrary φ), we adapt the standard convention of spherical coordinates to have the pole at $\boldsymbol{n}_u = \begin{pmatrix}\pm 1 & 0 & 0\end{pmatrix}^{\mathsf{T}}$. The conversion back to Cartesian coordinates then becomes

$$\boldsymbol{n}_u = \begin{pmatrix}\cos(\theta) \\ \sin(\theta)\cos(\varphi) \\ \sin(\theta)\sin(\varphi)\end{pmatrix}. \tag{S18}$$

By restricting both angles to the range $\theta, \varphi \in (0, \pi)$ we assume the tissue surface $\mathcal{S}_u$ to have normal vectors lying only on the upper hemisphere.

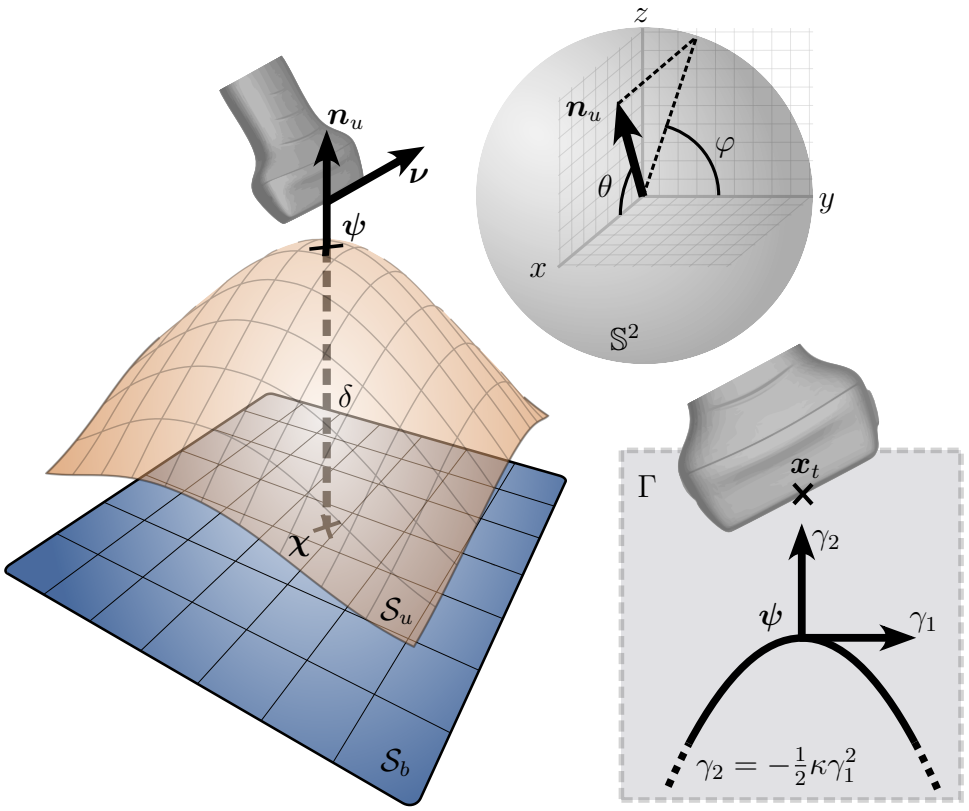


Fig. S11. **UKF state vector.** The state vector comprises the height δ of $\mathcal{S}_u$ relative to $\mathcal{S}_b$ at the contact point, the normal curvature κ of $\mathcal{S}_u$ in the plane Γ, and the spherical coordinates θ, φ of the corresponding unit normal vector.

c) Measurement vector: We choose the measurement

$$\boldsymbol{z} = \begin{pmatrix} c \\ s \end{pmatrix} \in [0,1] \times [-1,1], \tag{S19}$$

with c and s being the coverage and symmetry of acoustic coupling as derived in (3). Fig. S12a visualizes the measurements. The coverage has its maximum $c = 1$ when all scanlines show acoustic coupling, while being zero when the ultrasound probe is nowhere in contact with the tissue. Thus, c is an indication of good image quality. The symmetry s becomes maximal or minimal when acoustic coupling is affecting only one half of the ultrasound image. It therefore provides information about the in-plane orientation of the ultrasound probe, with $s = 0$ indicating good alignment.

d) Process model: Since this work deals with probe landing on a single point on the tissue, it is fair to assume the states $(\delta, \theta, \varphi)$ constant. The normal curvature κ generally changes with ultrasound probe orientation β for the same contact point: for distinct principal curvatures rotating the probe around the surface normal will change the normal curvature. However, we assume no prior knowledge on the curvature tensor and thus have no information on the rate of change $\partial\kappa/\partial\beta$. Hence, we assume κ quasi-stationary and the process model (S7) is simply

$$\hat{\boldsymbol{p}}_k^- = \hat{\boldsymbol{p}}_{k-1} + \boldsymbol{w}_{k-1}. \tag{S20}$$

e) Measurement model: The measurement model provides expected measurements $\hat{\boldsymbol{z}}_k = h(\hat{\boldsymbol{p}}_k^-)$ based on the a-priori state prediction $\hat{\boldsymbol{p}}_k^-$ from (S20). Fig. S12b visualizes the mathematical introduction of the measurement model. The goal is to calculate a w-tuple of binary numbers $\hat{\boldsymbol{a}}_k$ in accordance with (1), (2) that estimates the presence of acoustic coupling given $\hat{\boldsymbol{p}}_k^-$. We omit the time indices for brevity in the following calculations.

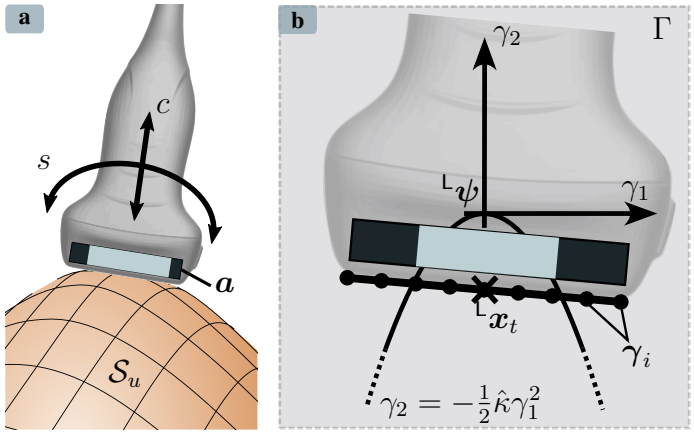


Fig. S12. **UKF measurement vector and model. (a)** The UKF measurements encode information on acoustic shadow in the ultrasound image in two scalar quantities c and s. **(b)** Discretizing the scan axis of the ultrasound probe into $\boldsymbol{\gamma}_i$ points and comparing each to the parabola locally describing $\mathcal{S}_u$ in the plane Γ provides estimated measurements $\hat{\boldsymbol{z}}$.

Express $\boldsymbol{\nu}$ in the local coordinate system $\{\mathsf{L}\}$ by choosing the orthogonal projection of $\boldsymbol{\nu}$ onto the tissue normal $\hat{\boldsymbol{n}}_u$ (their dot product) as γ_2-coordinate and setting the γ_1-coordinate to obtain a unit vector

$$ {}^{\mathsf{L}}\boldsymbol{\nu} = \begin{pmatrix} {}^{\mathsf{L}}\nu_1 \\ {}^{\mathsf{L}}\nu_2 \end{pmatrix} = \begin{pmatrix} \sqrt{1-(\boldsymbol{\nu}^{\mathsf{T}}\hat{\boldsymbol{n}}_u)^2} \\ \boldsymbol{\nu}^{\mathsf{T}}\hat{\boldsymbol{n}}_u \end{pmatrix} \in \mathbb{R}^2. \tag{S21} $$

Set the TCP of the ultrasound probe $\boldsymbol{x}_t$ to be the center of the probe elements at the tip of the probe and express it in local coordinates ${}^{\mathsf{L}}\boldsymbol{x}_t = (0, \hat{d}_u)^{\mathsf{T}}$, with

$$ \hat{d}_u = \begin{pmatrix} 0 & 0 & z_t - \hat{\delta} \end{pmatrix} \hat{\boldsymbol{n}}_u = (z_t - \hat{\delta}) \sin(\hat{\theta}) \sin(\hat{\varphi}) \tag{S22} $$

being the estimated distance to $\mathcal{S}_u$. For a linear ultrasound probe of length l, we calculate w points (w being the width of the ultrasound image $\boldsymbol{\mathcal{I}}_{(w\times h)}$) along the probe axis

$$ \boldsymbol{\gamma}_i = {}^{\mathsf{L}}\boldsymbol{x}_t + \varepsilon_i {}^{\mathsf{L}}\boldsymbol{\nu} \tag{S23} $$

$$ \varepsilon_i = \frac{l(i-1)}{(w-1)} - \frac{l}{2}, \quad i = 1 \dots w. \tag{S24} $$

Then, $\hat{\boldsymbol{a}}$ becomes

$$ \hat{a}_i = \begin{cases} 1 & \text{if } -\frac{1}{2}\hat{\kappa}\gamma_{i,1}^2 > \gamma_{i,2} \\ 0 & \text{otherwise} \end{cases} \quad i = 1 \dots w. \tag{S25} $$

Essentially, for each point $\boldsymbol{\gamma}_i$ along ${}^{\mathsf{L}}\boldsymbol{\nu}$ it is checked whether it lies below or above the surface parabola, with a point being below indicating tissue contact and hence good acoustic coupling along that scanline. Similarly, for a convex probe with curvature κ_p and width l, the measurement model can be derived by replacing (S23) with

$$ \boldsymbol{\gamma}_i = {}^{\mathsf{L}}\boldsymbol{x}_t + \varepsilon_i {}^{\mathsf{L}}\boldsymbol{\nu} + \frac{1}{2}\kappa_p \varepsilon_i^2 {}^{\mathsf{L}}\tilde{\boldsymbol{z}}, \quad i = 1 \dots w, \tag{S26} $$

with ${}^{\mathsf{L}}\tilde{\boldsymbol{z}}$ being the ultrasound probe z-axis expressed in $\{\mathsf{L}\}$. This generalizes to a linear ultrasound probe through $\kappa_p = 0$.

With $\hat{\boldsymbol{a}}$, the expected measurements $\hat{c}$ and $\hat{s}$ are calculated according to (3).

Given the UKF locally describes the planar section of $\mathcal{S}_u$ using a parabola (S17), implementing a rotational trajectory in β essentially results in an osculating paraboloid $\hat{\mathcal{S}}_u$ as a local estimate of $\mathcal{S}_u$ around $\boldsymbol{\psi}$.

D. Acoustic coupling detection

For identifying the probe-tissue contact quality, we perform image processing on the ultrasound images and provide information to the control system for optimization of the contact coupling. The method used in this work is based on [S14], which produces a discrete representation of the tissue within the ultrasound image in form of a sparse point cloud. Through this, it is possible to construct a confidence map of the perceptual quality of the image and detect contact-related acoustic shadow artifacts. The algorithm is capable of detecting acoustic shadow per scanline across the ultrasound image. See Fig. S13 for a visualization of the algorithm described in the following.

Remember the original ultrasound image $\boldsymbol{\mathcal{I}}_{w\times h}$ of width w and height h. For brevity, with a slight abuse of notation we denote $\boldsymbol{\mathcal{I}}_{w\times h} = \boldsymbol{\mathcal{I}}$ in this section. To detect contact-related acoustic shadow, first, areas of dynamic intensity change are detected through iterative Gaussian filtering ($n_f = 5$) following

$$\begin{aligned} \boldsymbol{\mathcal{I}}^{(i)} &= h_f * \boldsymbol{\mathcal{I}}^{(i-1)} \quad i = 1 \dots n_f \\ h_f &= \left(\frac{1}{\sqrt{2\pi\sigma_u}} e^{-u^2/(2\sigma_u^2)}\right)\left(\frac{1}{\sqrt{2\pi\sigma_v}} e^{-v^2/(2\sigma_v^2)}\right), \end{aligned} \tag{S27}$$

with $\boldsymbol{\mathcal{I}}^{(0)} = \boldsymbol{\mathcal{I}}$ and (u, v) the pixel coordinates of each image. The filter parameters are $\sigma_u = 0.2, \sigma_v = 1.8$. Vertical bias of the Gaussian filter, i.e. $\sigma_v \gg \sigma_u$, to be more sensitive to anatomical changes along the vertical direction. Let $\boldsymbol{\mathcal{I}}_{uv} = \boldsymbol{\mathcal{I}}(u, v)$ denote the pixel value of $\boldsymbol{\mathcal{I}}$ at coordinate (u, v). By calculating the per-pixel standard deviation across all filtered images $\boldsymbol{\mathcal{I}}^{(i)}$ (cf. S27)

$$\begin{aligned} \bar{\boldsymbol{\mathcal{I}}}_{uv} = \frac{1}{n_f}\sum_{i=1}^{n_f} \boldsymbol{\mathcal{I}}^{(i)}_{uv}, \;\; S_{uv} &= \sqrt{\frac{1}{n_f}\sum_{i=1}^{n_f}\left(\boldsymbol{\mathcal{I}}^{(i)}_{uv} - \bar{\boldsymbol{\mathcal{I}}}_{uv}\right)^2} \\ \boldsymbol{S}_{w\times h} &\coloneqq \{S_{uv} \mid (u, v) \in \{1 \dots w\} \times \{1 \dots h\}\}, \end{aligned} \tag{S28}$$

areas of more significant echogenic diversity produce larger intensity outputs. Using a predetermined threshold, a dense 2D point cloud discretizing the ultrasound image is constructed through

$$\Lambda_d \coloneqq \{(u, v) \mid S_{uv} \geq 4\}. \tag{S29}$$

To reduce computation, the point cloud undergoes a sparsification process using an inverse Gaussian density map to determine a set of weights $\boldsymbol{W}_{w\times h}$ of minimum distance for distances to a point.

Using this weight array, the point cloud (S29) is sparsified according to

$$\Lambda_s = \{\lambda_i \in \Lambda_d \mid \forall \lambda_j \in \Lambda_d, j \neq i : \|\lambda_j - \lambda_i\|_2 > W_{\lambda_i}\}. \tag{S30}$$

Here, W_{λ_i} is the weight in $\boldsymbol{W}_{w\times h}$ corresponding to the coordinate of the point $\lambda_i \in \Lambda_d$. Equation (S30) is repeated until all points are separated by their corresponding distances.

Finally, a simplicial complex, i.e., a set of points, edges, triangles, etc., is constructed over the sparsified point cloud (S30). Specifically, due to its simplicity and lack of optimization, a Vietoris–Rips complex is constructed. A Vietoris-Rips complex $\mathcal{VR}(\Lambda_s)$ is a collection of finite subsets of points in Λ_s, such that the pair-wise distance between every element in a subset of $\mathcal{VR}$ is not greater than a given threshold r. Define

$$\mathcal{VR}_n \coloneqq \{\Lambda \subset \mathcal{VR}(\Lambda_s) \mid |\Lambda| = n\} \tag{S31}$$

to be the set of all possible subsets of $\mathcal{VR}(\Lambda_s)$ of size n. Any subset of size n in a Vietoris-Rips complex describes a simplex of order $n - 1$. Consider for example

$$\begin{aligned} \mathcal{VR}_1 &= \{\bullet \subset \mathcal{VR}(\Lambda_s) \mid |\bullet| = 1\} \\ \mathcal{VR}_2 &= \{/ \subset \mathcal{VR}(\Lambda_s) \mid |/| = 2\} \\ \mathcal{VR}_3 &= \{\Delta \subset \mathcal{VR}(\Lambda_s) \mid |\Delta| = 3\} \end{aligned}$$

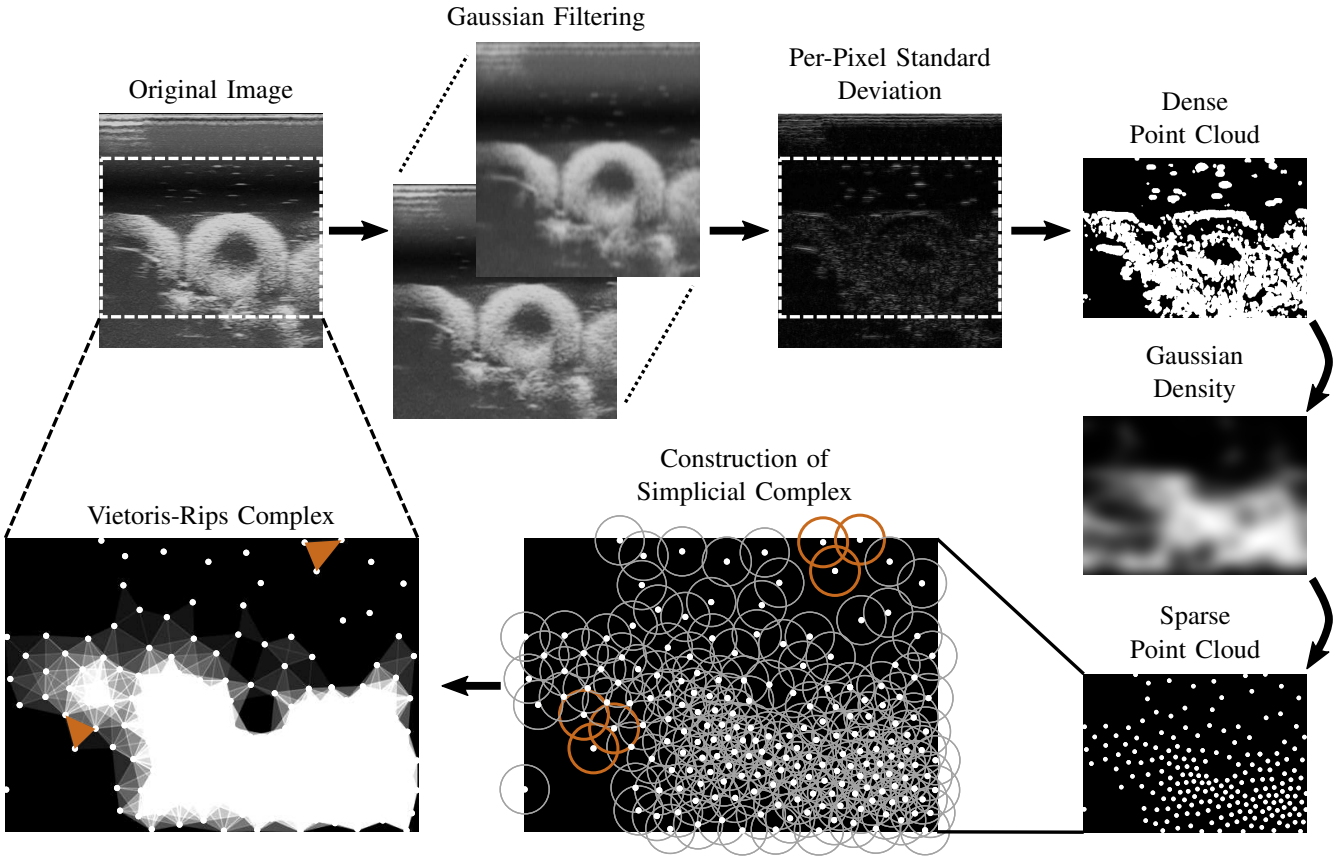


Fig. S13. Ultrasound image quality analysis to identify acoustic shadow. Iterative Gaussian filtering and calculation of per-pixel standard deviation results in a dense point cloud. Sparsification following Gaussian density and construction of a Vietoris-Rips complex leads to a discrete representation of visible tissue within the image. Acoustic shadow is a binary classification based on overlapping triangles along a scanline.

$\mathcal{VR}_1$ describes all 0-simplexes in $\mathcal{VR}$, meaning the points in Λ_s itself. Correspondingly, $\mathcal{VR}_2$ comprises all edges, $\mathcal{VR}_3$ contains all 2-simplexes or triangles. Remember that every subset in $\mathcal{VR}_n$ consists of n elements, and every subset has a diameter at most r.

From this discrete map of the visible tissue in the form of $\mathcal{VR}_3(\Lambda_s)$, acoustic shadow can be classified per scan line as binary w-tuple $\boldsymbol{a} \in \{0,1\}^w$. We define a scan line to be the u-th column of the original image

$$\boldsymbol{\mathcal{I}}_u = \boldsymbol{\mathcal{I}}(u) \coloneqq \{\boldsymbol{\mathcal{I}}_{uv} \subset \boldsymbol{\mathcal{I}} \mid v = 1 \dots h\}. \tag{S32}$$

Acoustic coupling is then classified via analysis of the number of 2D simplexes (triangles) intersecting a scanline

$$a_u = 1 \iff |\{\Delta \in \mathcal{VR}_3 : \Delta \cap \boldsymbol{\mathcal{I}}_u \neq \varnothing\}| \geq 2, \tag{S33}$$

for all scanlines $u = 1 \dots w$. Acoustic coupling, i.e., the absence of acoustic shadow, defined as a classification of 1, is conditional to when this number is above a pre-defined threshold.

E. Servoing Synthesis

The complete ultrasonic servoing control loop is visualized in Fig. S14 and consists of three main sections. The innermost control loop (cf. blue area in Fig. S14) controls the robot manipulator, with torques $\boldsymbol{\tau}$ provided by the surface-centric impedance controller (cf. Supplementary B-B). The UKF, which reads measurements $\boldsymbol{z}$ from the ultrasound probe and approximates the tissue surface locally through the state vector $\hat{\boldsymbol{p}}$, is represented by the orange area in Fig. S14. The local surface estimate $\hat{\mathcal{S}}_u$ is updated after each filter iteration, which is limited by the frame rate of the ultrasound machine and the rate at which

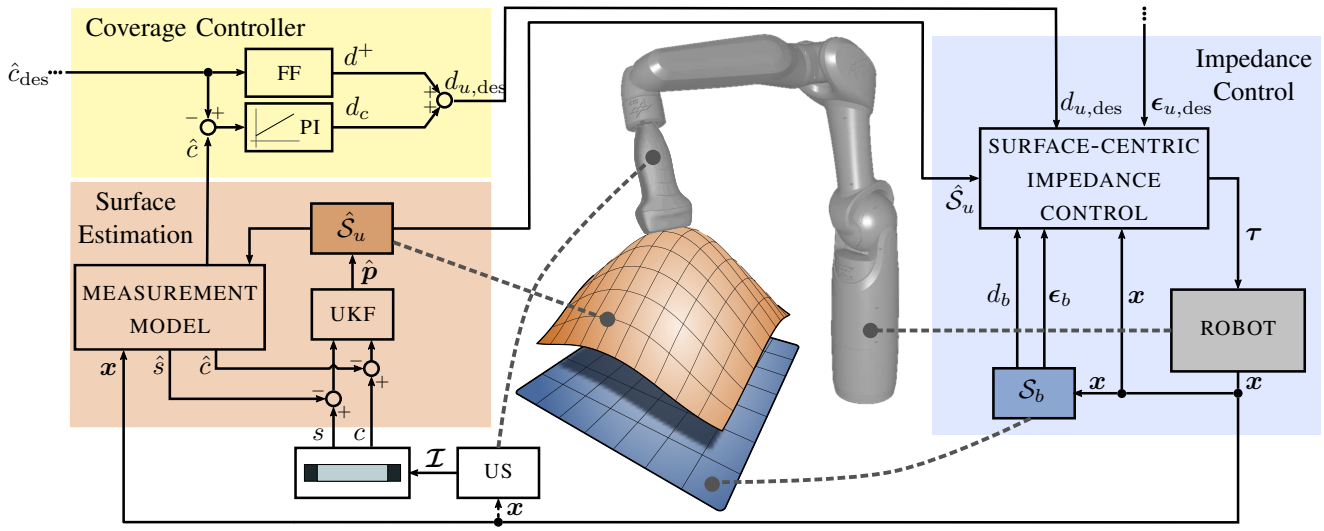


Fig. S14. **Closed loop ultrasonic servoing control.** The surface-centric impedance control provides torques to the robot necessary to establish contact between ultrasound (US) probe and the unknown tissue surface $\mathcal{S}_u$ (blue area). It does so based on the local surface estimate $\hat{\mathcal{S}}_u$ provided by the UKF (orange area). The commanded distance to achieve a desired extent of contact with the tissue is provided by the coverage controller acting on $\hat{c}$ (yellow area).

the acoustic coupling tuple (1) is calculated. To smoothen the discrete state updates of the UKF, we add a low-pass filter operating on the estimated states $\hat{\boldsymbol{p}}$ with a cutoff frequency of 1 Hz. Based on $\hat{\mathcal{S}}_u$, the surface-centric impedance control calculates torques necessary to guide the ultrasound probe along the unknown tissue surface $\mathcal{S}_u$. We describe the estimated surface paraboloid $\hat{\mathcal{S}}_u$ in a local coordinate frame $\{\mathsf{S}\}$ with origin $\hat{\boldsymbol{\psi}}$ and axes $\{\hat{\boldsymbol{X}}_{u,1}(\hat{\boldsymbol{\psi}}), \hat{\boldsymbol{X}}_{u,2}(\hat{\boldsymbol{\psi}}), \hat{\boldsymbol{n}}_u(\hat{\boldsymbol{\psi}})\}$ analytically as

$$ {}^{\mathsf{S}}z = -\left(\frac{\hat{\kappa}_1}{2}\,{}^{\mathsf{S}}x^2 + \frac{\hat{\kappa}_2}{2}\,{}^{\mathsf{S}}y^2\right). \tag{S34} $$

We keep track of the maximum and minimum estimated curvature $\hat{\kappa}$ during the UKF operation, to find the principal curvature directions $\hat{\boldsymbol{X}}_{u,1}(\hat{\boldsymbol{\psi}}), \hat{\boldsymbol{X}}_{u,2}(\hat{\boldsymbol{\psi}})$ and their corresponding principal curvature values $\hat{\kappa}_1, \hat{\kappa}_2$. After each filter iteration, $\hat{\mathcal{S}}_u$ is updated to have its vertex at height $\hat{\delta}$, i.e., $\hat{\psi}_z = \hat{\delta}$, and its normal vector at $\hat{\boldsymbol{\psi}}$ aligned with $\hat{\boldsymbol{n}}_u(\hat{\boldsymbol{\psi}})$. With this, we are able to analytically find the proxy point $\hat{\boldsymbol{\chi}}_u \in \hat{\mathcal{S}}_u$, i.e., the point on the estimated paraboloid $\hat{\mathcal{S}}_u$ closest to $\boldsymbol{x}_t$, and the task coordinates in (5) change to

$$ \hat{\boldsymbol{\rho}}_u = \begin{pmatrix} \hat{\boldsymbol{u}}_u(\boldsymbol{q}) \\ \hat{d}_u(\boldsymbol{q}) \\ \hat{\boldsymbol{\epsilon}}_u(\boldsymbol{q}) \end{pmatrix}, \tag{S35} $$

with $\hat{d}_u(\boldsymbol{q}) = (z_t(\boldsymbol{q}) - \hat{\delta})\sin(\hat{\theta})\sin(\hat{\varphi})$ and $\hat{\boldsymbol{\epsilon}}_u(\boldsymbol{q})$ the vector part of the unit quaternion $\hat{\boldsymbol{h}}_u = [\hat{\lambda}_u, \hat{\boldsymbol{\epsilon}}_u]$ describing the orientation of the probe's longitudinal axis relative to the estimated tissue surface normal $\hat{\boldsymbol{n}}_u$. $\hat{\boldsymbol{u}}_u(\boldsymbol{q})$ are parametrization coordinates on $\hat{\boldsymbol{\chi}}_u \in \hat{\mathcal{S}}_u$.

To have the ultrasound probe aligned with the tissue normal, we set $\boldsymbol{\epsilon}_{u,\mathrm{des}} = \boldsymbol{0}$. By assuming the UKF converges to $\hat{\theta} \approx \theta, \hat{\varphi} \approx \varphi$, this is equivalent to realizing a $s = s_{\mathrm{des}} = 0$ for any rotational yaw angle β. As this work deals purely with contact establishment at a static point without moving along the tissue, we specify $\boldsymbol{u}_{u,\mathrm{des}} = \boldsymbol{0}$ to keep the ultrasound probe positioned at $\hat{\boldsymbol{\psi}}$.

a) Coverage controller: We propose setting the desired distance for the surface-centric impedance controller based on a desired coverage c_{des} between ultrasound probe and tissue by implementing a coverage controller (cf. yellow area in Fig. S14). To avoid needing to control the noisy sensor measurement, this desired coupling is specified for the expected measurement $\hat{c}$. Following (S17), the desired distance

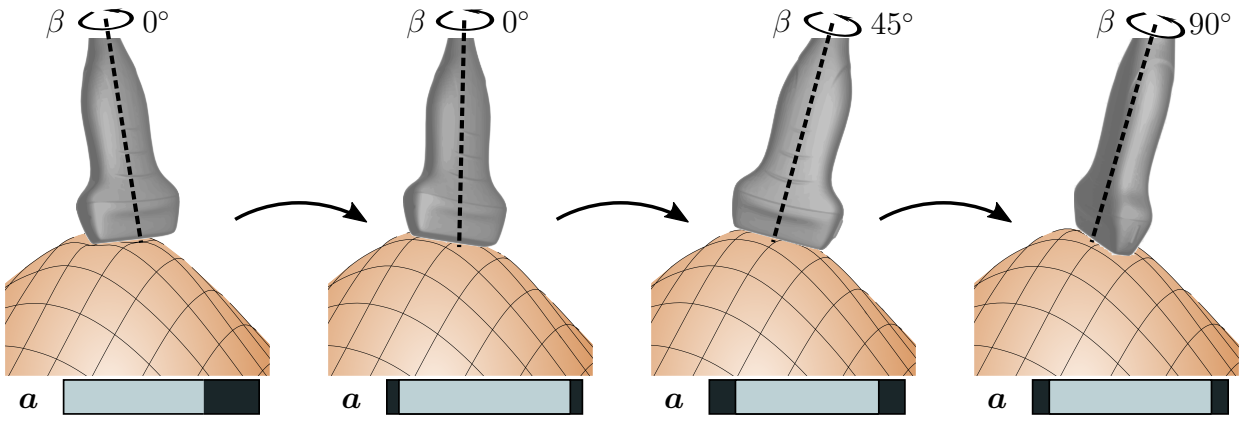


Fig. S15. **The proposed ultrasonic servoing control in action.** Symmetry of the tuple $\boldsymbol{a}$ gives information on the in-plane orientation of the ultrasound probe for a certain yaw angle β. Changing β while keeping $\boldsymbol{a}$ symmetrically distributed ensures the probe is aligned normal to the tissue.

to achieve a certain $\hat{c}_{\text{des}}$ for a linear ultrasound probe of length l, when the probe is aligned normal to the surface is given by the feedforward term

$$d^+ = -\frac{1}{2}\kappa \left(\frac{l}{2}\hat{c}_{\text{des}}\right)^2 = -\frac{l^2}{8}\kappa \hat{c}_{\text{des}}^2. \tag{S36}$$

We use the same feedforward term for a convex ultrasound probe, which is a sufficiently good approximation for small κ_p.

However, by setting $d_{\text{des}} = d^+$ it is not guaranteed that the ultrasound probe actually reaches a $d = d_{\text{des}}$, but rather settles at a distance where the passive interaction forces from controller and object stiffnesses equalize. Hence, we implement an additional PI controller to provide a correction term on the desired distance

$$d_c = k_p e_k + k_i \sum_{j=0}^{k} e_j, \tag{S37}$$

with $e_k = \hat{c}_{\text{des}} - \hat{c}_k$ at time t_k. With that the desired distance of the ultrasound probe becomes $d_{\text{des}} = d^+ + d_c$. The integrator in (S37) ensures that the robot is commanded a distance that results in a convergence to $d = d^+$, where $\hat{c} = c = \hat{c}_{\text{des}}$. To ensure safety, the PI controller (S37) saturates at $d_c = \pm 0.01$ m.

The robot guiding the ultrasound probe can be initialized arbitrarily above the target tissue. As initial state estimates at time $t = t_0$ we set $\hat{\delta}_0 = d_{b,0} + d^+ = z_{t,0} + d^+$, i.e., $\hat{\delta}$ is initialized such that $\hat{c}_0 = \hat{c}_{\text{des}}$ at the initial position $\boldsymbol{x}_{t,0}$ of the ultrasound probe. Correspondingly, $\hat{\boldsymbol{\psi}}_0 = \begin{pmatrix} x_{t,0} & y_{t,0} & \hat{\delta}_0 \end{pmatrix}^\mathsf{T}$. Furthermore, the initial values for $\hat{\theta}_0, \hat{\varphi}_0$ are such that $\hat{\boldsymbol{n}}_{u,0}$ is aligned with the initial z-axis $\tilde{\boldsymbol{z}}_0$ of the ultrasound probe. Lastly, we specify $\hat{\kappa}_0 = 1$, assuming the target tissue to have convex curvature. The yaw angle β is initialized such that $\boldsymbol{\nu}_0$ corresponds to $\beta_0 = 0°$.

When establishing contact, the ultrasonic servoing impedance controller orients the probe to achieve in-plane perpendicularity, i.e., $s \approx 0$, and adjusts the penetration depth to realize a $c \approx \hat{c} \approx \hat{c}_{\text{des}}$. Rotation of the ultrasound probe (cf. Fig. S15 and objective $O_{2.2}$) initiates automatically when the UKF converged in the initial plane Γ_0, as soon as $\hat{\boldsymbol{y}}_k \approx \boldsymbol{0}$.

SUPPLEMENTARY REFERENCES

[S1] U. Seibold, B. Kübler, T. Bahls, R. Haslinger, and F. Steidle, "The dlr mirosurge surgical robotic demonstrator," in *The Encyclopedia of Medical Robotics*. World Scientific, 2019, ch. Chapter 5, pp. 111–142.

[S2] H. Morehouse, H. P. Thaker, and C. Persaud, "Addition of metamucil to gelatin for a realistic breast biopsy phantom," *Journal of ultrasound in medicine*, vol. 26, no. 8, pp. 1123–1126, 2007.

[S3] M. A. Branch, T. F. Coleman, and Y. Li, "A subspace, interior, and conjugate gradient method for large-scale bound-constrained minimization problems," *SIAM Journal on Scientific Computing*, vol. 21, no. 1, pp. 1–23, 1999.

[S4] A. Jacobson, D. Panozzo, et al., *libigl: A simple C++ geometry processing library*, https://libigl.github.io/, 2018.

[S5] T. Needham, *Visual differential geometry and forms: A mathematical drama in five acts*. Princeton: Princeton University Press, 2021.

[S6] M. Dyck, A. Sachtler, J. Klodmann, and A. Albu-Schäffer, "Impedance control on arbitrary surfaces for ultrasound scanning using discrete differential geometry," *IEEE Robotics and Automation Letters*, vol. 7, no. 3, pp. 7738–7746, 2022.

[S7] N. Hogan, "Impedance control: An approach to manipulation," in *1984 American Control Conference*, 1984, pp. 304–313.

[S8] O. Khatib, "A unified approach for motion and force control of robot manipulators: The operational space formulation," *IEEE Journal on Robotics and Automation*, vol. 3, no. 1, pp. 43–53, 1987.

[S9] A. Albu-Schäffer, C. Ott, U. Frese, and G. Hirzinger, "Cartesian impedance control of redundant robots: Recent results with the DLR-light-weight-arms," in *2003 IEEE International conference on robotics and automation*, IEEE, vol. 3, 2003, pp. 3704–3709.

[S10] E. Wan and R. Van Der Merwe, "The unscented kalman filter for nonlinear estimation," in *Proceedings of the IEEE 2000 Adaptive Systems for Signal Processing, Communications, and Control Symposium (Cat. No.00EX373)*, 2000, pp. 153–158.

[S11] S. J. Julier and J. K. Uhlmann, "New extension of the kalman filter to nonlinear systems," in *Signal processing, sensor fusion, and target recognition VI*, Spie, vol. 3068, 1997, pp. 182–193.

[S12] R. Van der Merwe and E. Wan, "The square-root unscented kalman filter for state and parameter-estimation," in *2001 IEEE International Conference on Acoustics, Speech, and Signal Processing. Proceedings (Cat. No.01CH37221)*, vol. 6, 2001, pp. 3461–3464.

[S13] R. D. Turner, "Gaussian processes for state space models and change point detection," Ph.D. dissertation, Apollo - University of Cambridge Repository, Cambridge, UK, 2012.

[S14] A. Weld et al., "Identifying visible tissue in intraoperative ultrasound: A method and application," *International Journal of Computer Assisted Radiology and Surgery*, vol. 20, no. 10, pp. 2107–2117, 2025.